PHOTONICS Research

Ultrawide dynamic modulation of perfect absorption with a Friedrich–Wintgen BIC

Enduo Gao,[1] Rong Jin,[2] Zhenchu Fu,[2] Guangtao Cao,[3,6] Yan Deng,[4] Jian Chen,[2] Guanhai Li,[2,5,*] Xiaoshuang Chen,[2] and Hongjian Li[1,7]

[1]School of Physics and Electronics, Central South University, Changsha 410083, China
[2]State Key Laboratory of Infrared Physics, Shanghai Institute of Technical Physics, Chinese Academy of Sciences, Shanghai 200083, China
[3]School of Physics and Electronic Sciences, Changsha University of Science and Technology, Changsha 410004, China
[4]School of Physics and Chemistry, Hunan First Normal University, Changsha 410205, China
[5]Hangzhou Institute for Advanced Study, University of Chinese Academy of Sciences, Hangzhou 310024, China
[6]e-mail: caoguangtao456@126.com
[7]e-mail: lihj398@126.com
*Corresponding author: ghli0120@mail.sitp.ac.cn

Received 23 November 2022; revised 26 December 2022; accepted 4 January 2023; posted 5 January 2023 (Doc. ID 481020); published 1 March 2023

Dynamical control of perfect absorption plays an indispensable role in optical switch and modulators. However, it always suffers from the limited modulation range, small depth, and susceptible absorption efficiencies. Here, we propose a new strategy based on Friedrich–Wintgen bound states in the continuum (F–W BICs) to realize a tunable perfect absorber with large dynamic modulation range. For proof of concept, we demonstrate a pentaband ultrahigh absorption system consisting of graphene gratings and graphene sheets through elaborately tuning F–W BIC. The nature of the F–W BIC arises from the destructive interference between Fabry–Perot resonance and guided mode resonance modes in the coherent phase-matching condition. The radiation channels are avoided from crossing. The BIC can be dynamically modulated by engineering the Fermi level of graphene gratings, which breaks the traditional modulation methods with an incidence angle. Remarkably, the perfect absorber with this F–W BIC approach achieves the largest modulation range of up to 3.5 THz. We believe that this work provides a new way to dynamically engineer perfect absorption and stimulates the development of multiband ultracompact devices.

https://doi.org/10.1364/PRJ.481020

1. INTRODUCTION

Surface plasmon polaritons (SPPs), which are generated by the coupling between photons in the incident light source and electrons on a metal or insulator, can break the diffraction limit of conventional optics and localize light in the subwavelength range. Thus, SPP-based metamaterials hold potential applications in sensing, imaging, and communications [1–3]. In particular, SPP-based perfect absorbers have been widely studied, such as the dual-band absorber based on the dielectric grating and Fabry–Perot cavity [4], the narrowband absorber based on multiridge gratings [5], and the broadband absorber based on tungsten ring-disc array [6]. However, the majority of absorbers can only be statically regulated, seriously hindering their practical application. Graphene, due to its ultracompact configuration, low loss, and flexible tunability, has become the research focus. In general, perfect absorption can be achieved when the radiation loss and absorption loss of the graphene system are equal [7]. The variation of the Fermi level of graphene inevitably leads to the difference between radiation loss and absorption loss. In addition, as the Fermi level of graphene decreases, the coupling between the in-plane electric field and the interband absorption of graphene becomes weaker, resulting in a lower absorption rate of the system [8–16]. Thus, it is a challenge to ensure the perfect absorption of the system while dynamically regulating the frequency. Despite the fact that a small number of devices can obtain perfect absorption of dynamic regulation, the frequency modulation range is less than 2 THz [17–22].

Originally derived from the quantum theory, the bound states in the continuum (BICs) refer to the isolated eigenvalues of the single-particle Schrödinger equation of positive energy states in the continuum [23]. Subsequently, it was extended to many fields, such as electromagnetism [24], acoustics [25], fluid dynamics [26], and optics [27]. The optical BICs behave as a resonant state with zero linewidth and infinite quality factor (Q-factor). Kivshara *et al.* discussed the potential

mechanism of the optical BIC [28] and proposed a polarization-insensitive quasi-BIC [29]. This feature was verified experimentally in the transmission of the metasurfaces. Remarkably, the optical BIC is employed into the field to generate higher harmonics up to the 11th order [30]. An accidental BIC is the unexpected disappearance of the coupling between the bound state and the continuum by tuning the parameters of the system [31,32]. It can be subdivided into the Fabry–Perot (F–P) BIC [33] and Friedrich–Wintgen (F–W) BIC [34]. The F–P BIC arises from the destructive interference between two identical resonant modes when the phase difference between them is an integer multiple of π. The F–W BIC occurs from a destructive interference between two different excitation modes, and their radiation channels avoid crossing. However, it is worth noting that in the modulation of the F–W quasi-BIC, one mode gradually disappears to form the BIC, and the other mode changes to a limited extent due to the complicated underlying physics [35–37]. Until now, introducing the F–W BIC tuned by the Fermi level to achieve the dynamic modulation of perfect absorption remains unresolved and is very desirable.

In this work, we propose a new strategy to realize a tunable perfect absorption based on F–W BICs. First, a pentaband ultrahigh absorber arising from the interaction of Fabry–Perot resonance (FPR) and guided mode resonance (GMR) is demonstrated. The absorption rates of three modes in the pentaband absorber are higher than 98%, which are far better than other single-band [38,39], dual-band [40–44], and multiband [45–48] absorbers. Further studies show that statically modulating the width of graphene gratings can lead to a strong coupling between FPR and GMR modes, resulting in an F–W BIC. Theoretical analysis based on the coupled-mode theory (CMT) [49,50] reveals the strong coupling between the two modes and fits well with the absorption spectrum of the numerical simulation. To demonstrate the BIC, the band structure of the proposed system is shown, with the real part of the complex frequency of the BIC coinciding with the BIC position of the absorption spectrum. The free-space radiation in the field distribution of the BIC is zero, which further proves that the F–W BIC is an eigenstate of the system. Furthermore, the F–W BIC realized by the dynamic modulation of the Fermi level of graphene gratings can break the traditional modulation with the incidence angle. Most interestingly, thanks to the formation of the F–W BIC, the like-FPR mode can be dynamically modulated while ensuring its perfect absorption. The modulation range is up to 3.5 THz, which is much higher than that of other perfect absorbers [17–22].

2. STRUCTURAL DESIGN AND ANALYSIS

Figure 1 represents the proposed model. The monolayer graphene is sandwiched in the dielectric, the graphene grating is placed on top, and the substrate is gold. The graphene surface conductivity can be expressed as [51]

$$\sigma_g = \frac{ie^2 E_F}{\pi\kappa^2(\omega + i\tau^{-1})}, \tag{1}$$

where ω is the angular frequency of the light source, E_F is the graphene Fermi level, e is the electron charge, κ is the reduced Planck constant, and τ is the carrier relaxation time, which can

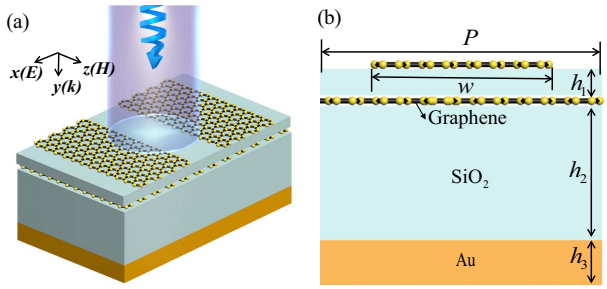

Fig. 1. (a) 3D schematic diagram composed of graphene gratings and graphene sheets; (b) 2D side view of the proposed system; the specific parameters are as follows: $P = 490$ nm, w = 400 nm, $h_1 = 12$ nm, $h_2 = 1350$ nm, $h_3 = 100$ nm, $E'_f = E_f = 1.0$ eV.

be represented by $\tau = \mu E_f/(ev_F^2)$. The Fermi velocity and carrier mobility of the system are $v_F = 10^6$ m/s and $\mu = 1\ \mathrm{m^2/(V \cdot s)}$, respectively [52]. A side view of the system is plotted in Fig. 1(b) to show the structure more clearly. The period of the structural unit is $P = 490$ nm, the width of the graphene grating is $w = 400$ nm, the refractive index of the SiO_2 is $n = 1.6$, and the distance between the graphene grating and graphene sheet is $h_1 = 12$ nm. Since the carrier concentration of single-layer graphene can be as high as $4 \times 10^{18}\ \mathrm{m^{-2}}$, the Fermi level of graphene can reach 1.17 eV [53]. Thus, the Fermi level E'_f of graphene gratings and the Fermi level E_f of graphene sheets are set to a maximum of 1.0 eV.

In this paper, the finite-difference time-domain (FDTD) method is adopted to explore the absorption spectrum of the proposed system. A transverse magnetic (TM) wave is used as an excitation source to irradiate the system vertically. The Bloch period condition and the perfectly matched boundary are set in the x direction and y direction, respectively. The simulation temperature and time are 300 K and 8000 fs, respectively. Mesh accuracy is 5 nm in both the x and y directions. The gold mirror is used to block the transmission of TM waves, so the absorption of the system is $A = 1 - R$.

3. SIMULATION RESULTS AND DISCUSSION

Since an F–W BIC is a strong coupling between two modes, we first analyze the specific mode. The TM-polarized wave as an excitation source can produce an excellent pentaband absorber with absorption rates above 90%, of which three bands are as high as 98% or more, as shown in Fig. 2(a). Since the impedance mismatch between the regions with and without an upper graphene grating, the graphene surface plasmon polaritons (GSPPs) propagating along the x direction reflect back and forth between the two boundaries, forming a standing wave. For visual observation, the positive and negative charges of the electric field distribution are represented by "+" and "–." This standing wave can also be called lateral FPRs [54], which can be expressed as

$$\omega_{\mathrm{FPR}} = \frac{\mathrm{Kc}}{2wn_M}. \tag{2}$$

Here, n_M is the effective refractive index of the standing wave, and c is the light velocity. K, corresponding to the mode order

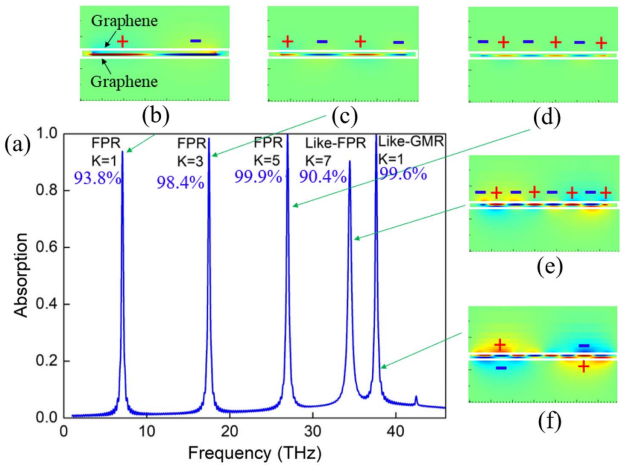

Fig. 2. (a) Absorption spectra of the proposed system; (b)–(f) electric field distribution of different modes in the y direction.

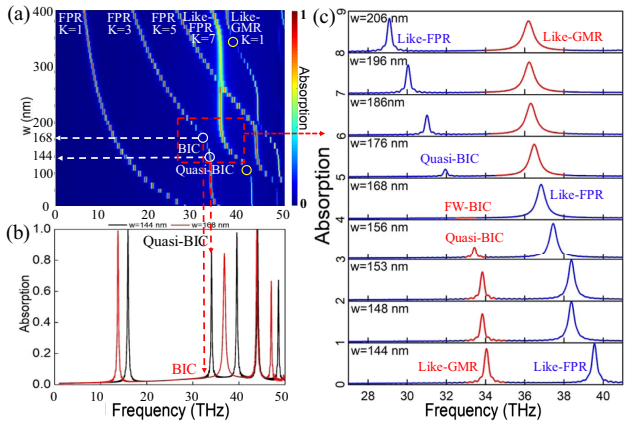

Fig. 3. BIC formation in the hybrid FPR–GMR system. (a) Absorption spectrum as a function of the width of the graphene grating; (b) cross sections of the absorption spectra at $w = 168$ nm and 144 nm show the appearance of the collapsed F–W BIC to quasi-BIC. (c) Avoided crossing and linewidth vanishing due to the coupling of FPR and GMR modes at different w.

of the FPR mode, is the number of the electric field nodes [Figs. 2(b)–2(e)], which is equal to integer multiples of the half-wavelength. The vertically incident TM-polarized light can only excite the odd mode of the FPR because the effective charge dipole provides the restoring force for the collective oscillating wave [55]. In addition, graphene gratings enable momentum matching between incident light and GSPPs to excite GMR [Fig. 2(f)], which can be expressed as [56]

$$\omega_{\mathrm{GMR}} = \sqrt{\frac{e^2 E_F}{\kappa^2 \varepsilon_0 \varepsilon_r P}}. \tag{3}$$

Here, ε_0 is the permittivity in vacuum, and ε_r is the relative permittivity of the SiO_2.

To explore modes corresponding to different excitation mechanisms, the electric field diagrams of different modes in the y direction are shown in Figs. 2(b)–2(f). As we predicted, FPR modes are generated in the F–P cavities constructed from graphene gratings and graphene sheets, and the corresponding K are 1, 3, 5, 7, respectively. A first-order GMR mode appears on the outside of graphene gratings and graphene sheets. It is worth noting that the coupling between the FPR ($K = 7$) and the GMR ($K = 1$) modes occurs due to their close proximity, so those two modes are named like-FPR and like-GMR modes. The ultrahigh absorption of the system is mainly manifested by three aspects. On the one hand, the FPR resonance mode ($K = 1, 3, 5, 7$) interacts with graphene gratings and the graphene sheets to enhance the light absorption. On the other hand, the GMR mode excited by the graphene grating similarly enhances the absorption. In addition, the strong coupling between the FPR ($K = 7$) and GMR modes further enhances the light localization.

To observe the formation process of the F–W BIC, the absorption spectrum as a function of the width of the graphene grating is shown in Fig. 3(a). An avoided resonance crossing with a Rabi splitting is observed around 33 THz. Due to the destructive interference between FPR ($K = 3$) and GMR modes at the phase-matching conditions [57], an F–W BIC is generated at an off-Γ point. The hybridization of FPR and GMR modes forms a new polaritonic-optical quasi-particle [58,59]. In short, the nature of the F–W BIC is a destructive interference between two different resonance modes, and their radiation channels avoid crossing. The BIC at $w = 168$ nm and quasi-BIC (white circle) at $w = 144$ nm are denoted in Fig. 3(b). The yellow circle in Fig. 3(a) is also the strong coupling between the different modes, one of which does not completely disappear even though their radiation channels avoid crossing, which occurs because the two modes do not reach the suitable phase-matching condition. Therefore, the position of yellow circle also can achieve an F–W BIC by modulating the parameters to achieve the correct phase-matching conditions. The absorption spectra at different w [Fig. 3(c)] indicate an avoided crossing behavior with Rabi splitting. The Rabi energy can reach 18.9 meV when $w = 176$ nm [60].

The strong coupling between FPR and GMR modes can be resolved by CMT [Fig. 4(a)]. The A_n stands for the FPR or GMR mode, and its amplitude is a_n. $\gamma_{\mathrm{on}} = \omega_n/2Q_{\mathrm{on}}$ and $\gamma_{\mathrm{in}} = \omega_n/2Q_{\mathrm{in}}$ are the inter-external and inter-internal loss coefficients of the two modes. Q_{on} and Q_{in} are the inter-external and inter-internal loss quality factor, and they can be satisfied by $1/Q = 1/Q_{\mathrm{on}} + 1/Q_{\mathrm{in}}$ (Q is the total quality factor of quasi-BIC or like-FPR mode). The coupling coefficient between modes can be represented by μ_{12} and μ_{21}. $A_n^{\mathrm{in/out}}$ ($n = 1, 2$) indicates the incident or outgoing wave along the positive or negative direction of the mode. The interaction between the two modes can be represented as

$$\begin{pmatrix} \gamma_1 & -i\mu_{12} \\ -i\mu_{21} & \gamma_2 \end{pmatrix} \cdot \begin{pmatrix} a \\ b \end{pmatrix} = \begin{pmatrix} -\gamma_{o1}^{1/2} & 0 \\ 0 & -\gamma_{o2}^{1/2} \end{pmatrix} \cdot \begin{pmatrix} A_{1+}^{\mathrm{in}} + A_{1-}^{\mathrm{in}} \\ A_{2+}^{\mathrm{in}} + A_{2-}^{\mathrm{in}} \end{pmatrix}, \tag{4}$$

where $\gamma_{1(2)} = i\omega - i\omega_{1(2)} - \gamma_{i1(2)} - \gamma_{o1(2)}$. The coupling between FPR and GMR satisfies the energy conservation,

$$A_{2+}^{\mathrm{in}} = A_{1+}^{\mathrm{out}} e^{i\varphi}, \qquad A_{1-}^{\mathrm{in}} = A_{2-}^{\mathrm{out}} e^{i\varphi}. \tag{5}$$

Here, φ is the phase difference between the FPR and GMR modes. For one of two modes, energy conservation still holds, which can be expressed as

$$A_{n\pm}^{\text{out}} = A_{n\pm}^{\text{in}} - a_n \gamma_{\text{on}}^{1/2}, \qquad n = 1, 2. \tag{6}$$

Due to the presence of the substrate gold, the electromagnetic waves emitted from the GMR mode return to continue interacting with the one, which can be expressed as

$$A_{2-}^{\text{in}} = A_{2+}^{\text{out}} e^{2i\phi}. \tag{7}$$

Thus, the reflection coefficient r of the coupling system can be obtained by

$$r = \frac{A_{-}^{\text{out}}}{A_{+}^{\text{in}}} = e^{2i(\varphi+\phi)} - \frac{\gamma_{o1}^{1/2} a_1 [1 + e^{2i(\varphi+\phi)}] + \gamma_{o2}^{1/2} a_2 e^{i\varphi}(1 + e^{2i\phi})}{A_{+}^{\text{in}}}. \tag{8}$$

The specific coefficients are as follows:

$$\frac{a}{A_{+}^{\text{in}}} = \frac{\gamma_{o1}^{1/2}[1 + e^{2i(\varphi+\phi)}]k_2 - \gamma_{o1}^{1/2} e^{i\varphi}(1 + e^{2i\phi})}{k_1 k_2 + \chi_2}, \tag{9}$$

$$\frac{b}{A_{+}^{\text{in}}} = \frac{\gamma_{o2}^{1/2} e^{i\varphi}(1 + e^{2i\phi}) - \gamma_{o1}^{1/2} e^{i\varphi}[1 + e^{2i(\varphi+\phi)}]\chi_2}{k_1 k_2 + \chi_1 \chi_2}, \tag{10}$$

where

$$\chi_1 = i\mu_{12} + \gamma_{o1}^{1/2} \gamma_{o2}^{1/2} e^{i\varphi}(1 + e^{2i\phi}),$$
$$\chi_2 = i\mu_{21} + \gamma_{o1}^{1/2} \gamma_{o2}^{1/2} e^{i\varphi}(1 + e^{2i\phi}), \tag{11}$$

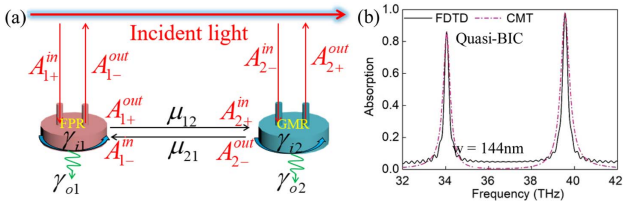

Fig. 4. (a) Schematic diagram of CMT; (b) coupled absorption spectra of FDTD numerical simulation and CMT fitting at $w = 400$ nm.

$$k_1 = \gamma_{o1} e^{2i(\varphi+\phi)} - \gamma_1,$$
$$k_2 = \gamma_{o2} e^{2i\phi} - \gamma_2. \tag{12}$$

Therefore, the absorption rate of the system is $A = 1 - r^2$. The coupled absorption spectrum between FPR and GMR modes at $w = 144$ nm is shown in Fig. 4(b), and the results of CMT are consistent with the data of the FDTD.

To demonstrate the F–W BIC, the band structures and the corresponding Q-factor evolution of the FPR–GMR hybrid system are plotted in Fig. 5. The band structures of the FPR and GMR modes avoid crossing, marking the formation of an F–W BIC [61]. The position of the band structure corresponding to the maximum value in the Q-factor evolution is BIC. The Q value is finite due to absorption loss. The real part of the corresponding complex frequency of the BIC at $k_x = 0.068$ is 33 THz, which is consistent with the position of the BIC in the boundary value problem [Fig. 3(b)]. Also, the electric field distribution of the BIC at $k_x = 0.068$ is represented in the inset of Fig. 5(a). The rapid decay of the far field of the eigenmode to 0 further demonstrates the BIC. Therefore, the F–W BIC of the proposed system is an eigenstate with 0 radiative loss, but it still has absorption loss.

To dynamically modulate the frequency in a graphene system while ensuring perfect absorption, the absorption loss and radiation loss of the system must be equal during the modulation. Thus, dynamic regulation of F–W BICs based on graphene perfect absorbers offers the possibility. In the proposed structure, E_f' of graphene gratings can be modulated by the gate voltage V_g, which can be expressed as [62]

$$E_f' = \kappa v_F \left(\frac{\pi \varepsilon_0 \varepsilon_r V_g}{h_1 e} \right)^{1/2}. \tag{13}$$

Here, ε_0 is the permittivity of free space. E_f of the graphene sheets, which is set to a constant value, does not require a gate voltage. Thus, we intend to achieve an F–W BIC by modulating the E_f' of the graphene grating. The absorption spectrum at $w = 144$ nm in Fig. 3(c) is employed as an example of dynamic modulation. As E_f' decreases, both GMR and FPR modes produce a redshift. The redshift of the GMR mode can be explained by Eq. (3). For the FPR mode, the reduction of graphene E_f' increases the effective refractive index n_M of the FPR mode [63], resulting in a redshift. The destructive interference between FPR and GMR modes at the appropriate phase matching produces an F–W BIC when $E_f' = 0.55$ eV. Field distributions of these two modes in the y direction when

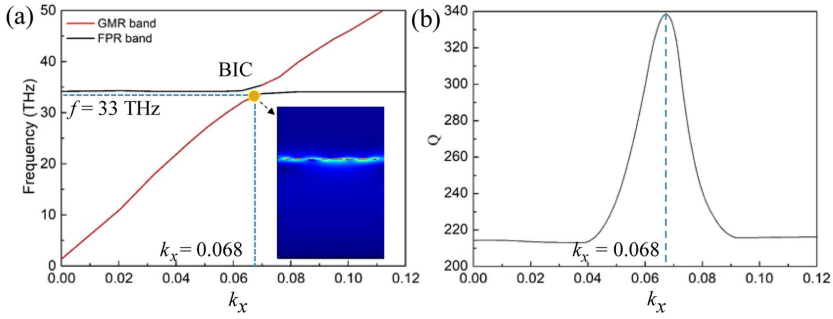

Fig. 5. (a) Band structures of the proposed FPR–GMR hybrid system. Here, the illustration shows electric field distribution at F-W BIC. (b) Simulated Q-factor evolution for the GMR band.

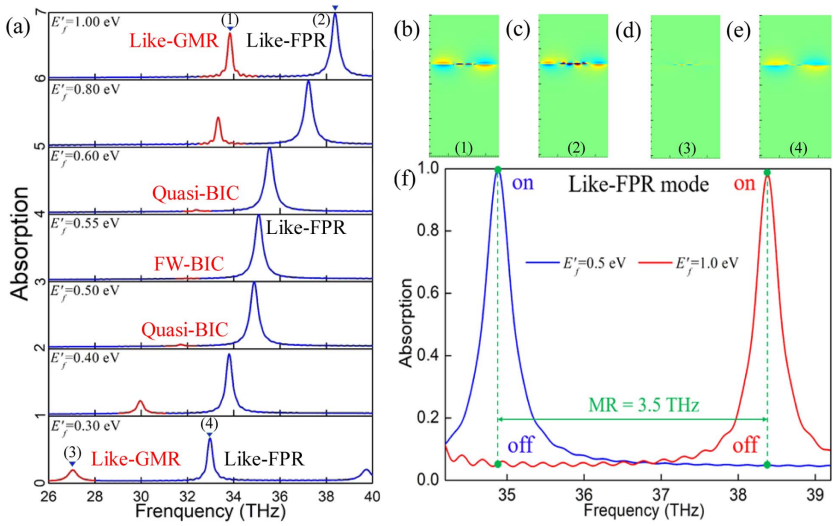

Fig. 6. (a) F–W BIC dynamically modulated by the Fermi energy level of a graphene grating ($w = 144$ nm); (b)–(e) field distribution of the two modes in the y direction when $E'_f = 1.0$ eV and 0.3 eV; (f) perfect absorption frequency modulator and optical switch based on F–W BIC.

$E'_f = 1.0$ eV and 0.3 eV are shown in Figs. 6(b)–6(e). It can be clearly observed that these two modes exchange energy before and after the strong coupling. In Fig. 6(f), the like-FPR mode achieves dynamic modulation at 34.88–38.38 THz while also obtaining perfect absorption due to the F–W BIC effect. The absorption rate of the like-FPR mode increases from 98.17% to 99.70% (near perfect absorption) when E'_f is reduced from 1.0 to 0.5 eV. The frequency modulation range (MR) of like-FPR mode can reach 3.5 THz, which is higher than the perfect graphene-based absorbers [17–22] that have been reported, as shown in Table 1. In addition, the switching of Fermi levels also enables a dual-frequency asynchronous switch. The parameters for evaluating the switch performance are mainly determined by the modulation depth (MD) and insertion loss (IL), which can be represented by $\mathrm{MD} = (A_{\max} - A_{\min})/A_{\max}$ and $\mathrm{IL} = -10\log_{10}(A_{\max})$, respectively. In addition, the dephasing time is also an important parameter that characterizes the sensitivity of the switch, which can be expressed by $\mathrm{DT} = 2\kappa/\Delta f$, with Δf being the full width at half-maximum [64]. The MD, IL, and DT of the dual-band asynchronous switch are 94.72%, 94.98%, 0.012 dB, 0.080 dB, 5.00 ps, and 5.88 ps, respectively. The high MD and DT and low IL indicate the excellent performance of the proposed switch. Therefore, based on the dynamically tunable F–W BIC, the like-FPR mode ensures its absorption while dynamical modulating and can also be applied to the dual-frequency asynchronous switch.

4. CONCLUSION

In summary, we have achieved dynamic modulation of the perfect absorption spectrum in a pentaband ultrahigh absorption system composed of graphene gratings and graphene sheets by introducing an F–W BIC. The radiation loss of the system is suppressed due to the destructive interference between FPR and GMR modes at coherent phase-matching conditions, producing an F–W BIC. Its nature originates from the avoidance of crossing when two different modes are coupled to the same radiation channel. Remarkably, the largest modulation range, 3.5 THz, is achieved by controlling the Fermi level of the graphene grating with our structure. It holds great promise in applications like optical switches and frequency modulators with perfect absorption. We believe this work will provide a new strategy to develop frequency modulators with perfect absorption and stimulate the development of multiband ultracompact devices.

Table 1. Comparisons among Perfect Absorbers

Reference/Year	Material Structure	Modulation Range	Physical Mechanism
[17]/2021	Metamaterials based on graphene cross and four graphene side stripes	0.4 THz	Plasmon-induced absorption
[18]/2021	Graphene-dielectric-metal structure	1.8 THz	Graphene surface plasmon resonance
[19]/2022	Graphene layers with four T-shaped stripes and a square ring pattern	0.5 THz	Graphene surface plasmon resonance
[20]/2022	Triangle graphene metamaterial	0.7 THz	FPR
[21]/2022	Dielectric multilayers integrated with graphene and VO_2	1.5 THz	Nonreciprocity of the dielectric graphene multilayers integrated with a VO_2 defect layer
[22]/2022	Metamaterials based on monolayer graphene and gold gratings	2 THz	GMR
This work	Graphene gratings and graphene sheets structure	3.5 THz	F–W BIC

Funding. Hunan Provincial Innovation Foundation for Postgraduate (1053320200208); Shanghai Municipal Science and Technology Major Project (2019SHZDZX01); Science and Technology Commission of Shanghai Municipality (20JC1416000, 22JC1402900); Shanghai Rising-Star Program (20QA1410400); Natural Science Foundation of Zhejiang Province (LR22F050004); Strategic Priority Research Program of Chinese Academy of Sciences (XDB43010200); Youth Innovation Promotion Association of the Chinese Academy of Sciences (Y2021070); National Natural Science Foundation of China (61865006, 61875218, 62222514, 91850208); National Key Research and Development Program of China (2018YFA0306200).

Disclosures. The authors declare that there are no conflicts of interest.

Data Availability. The data that support the findings of this study are available from the corresponding author on reasonable request.

REFERENCES

1. H. T. Chen, R. Kersting, and G. C. Cho, "Terahertz imaging with nanometer resolution," Appl. Phys. Lett. **83**, 3009–3011 (2003).
2. S. Pereira and S. LaRochelle, "Field profiles and spectral properties of chirped Bragg grating Fabry-Perot interferometers," Opt. Express **13**, 1906–1915 (2005).
3. H.-J. Song and T. Nagatsuma, "Present and future of terahertz communications," IEEE Trans. Terahertz Sci. Technol. **1**, 256–263 (2011).
4. F. Chen, H. Zhang, L. Sun, J. Li, and C. Yu, "Double-band perfect absorber based on the dielectric grating and Fabry–Perot cavity," Appl. Phys. A **125**, 792 (2019).
5. C. Fu, B. Wang, X. Zhu, Z. Xiong, and Y. Huang, "Narrowband absorbers based on multi-ridge gratings," Optik **257**, 168839 (2022).
6. Z. Yi, J. Li, J. Lin, F. Qin, X. Chen, W. Yao, Z. Liu, S. Cheng, P. Wu, and H. Li, "Broadband polarization-insensitive and wide-angle solar energy absorber based on tungsten ring-disc array," Nanoscale **12**, 23077–23083 (2020).
7. C. Qu, S. Ma, J. Hao, M. Qiu, X. Li, S. Xiao, Z. Miao, N. Dai, Q. He, S. Sun, and L. Zhou, "Tailor the functionalities of metasurfaces based on a complete phase diagram," Phys. Rev. Lett. **115**, 235503 (2015).
8. E. Gao, Z. Liu, H. Li, H. Xu, Z. Zhang, X. Luo, C. Xiong, C. Liu, B. Zhang, and F. Zhou, "Dynamically tunable dual plasmon-induced transparency and absorption based on a single-layer patterned graphene metamaterial," Opt. Express **27**, 13884–13894 (2021).
9. P. Sun, C. You, A. Mahigir, T. Liu, F. Xia, W. Kong, G. Veronis, J. P. Dowling, L. Dong, and M. Yun, "Graphene-based dual-band independently tunable infrared absorber," Nanoscale **10**, 15564–15570 (2018).
10. Q. Shangguan, H. Chen, H. Yang, S. Liang, Y. Zhang, S. Cheng, W. Yang, Z. Yi, Y. Luo, and P. Wu, "A 'belfry-typed' narrow-band tunable perfect absorber based on graphene and the application potential research," Diam. Relat. Mater. **125**, 108973 (2022).
11. P. Wu, X. Zeng, N. Su, M. Chen, Y. Zeng, and Y. Yu, "A graphene perfect absorber with tunable, dual band, high sensitivity characteristics," Diam. Relat. Mater. **125**, 109002 (2022).
12. H. Xu, C. X. Xiong, Z. Q. Chen, M. F. Zheng, M. Z. Zhao, B. H. Zhang, and H. J. Li, "Dynamic plasmon-induced transparency modulator and excellent absorber-based terahertz planar graphene metamaterial," J. Opt. Soc. Am. B **35**, 1463–1468 (2018).
13. A. B. Asl, D. Pourkhalil, A. Rostami, and H. Mirtaghioglu, "A perfect electrically tunable graphene-based metamaterial absorber," J. Comput. Electron. **20**, 864–872 (2021).
14. Y. Qi, C. Liu, B. Hu, X. Deng, and X. Wang, "Tunable plasmonic absorber in THz-band range based on graphene arrow-shaped metamaterial," Results Phys. **23**, 104044 (2021).
15. W. Liu and Z. Song, "Terahertz absorption modulator with largely tunable bandwidth and intensity," Carbon **174**, 617–624 (2021).
16. Z. Chen, H. Chen, H. Jile, D. Xu, Z. Yi, Y. Lei, X. Chen, Z. Zhou, S. Cai, and G. Li, "Multi-band multi-tunable perfect plasmon absorber based on L-shaped and double-elliptical graphene stacks," Diam. Relat. Mater. **115**, 108374 (2021).
17. J. Gong, X. Shi, Y. Lu, F. Hu, R. Zong, and G. Li, "Dynamically tunable triple-band terahertz perfect absorber based on graphene metasurface," Superlattices Microstruct. **150**, 106797 (2021).
18. T. Chen, W. Jiang, and X. Yin, "Dual-band ultrasensitive terahertz sensor based on tunable graphene metamaterial absorber," Superlattices Microstruct. **154**, 106898 (2021).
19. Y. Yuan, Y. Qi, B. Zhang, J. Ding, W. Liu, H. Chen, and X. Wang, "A polarization-insensitive, wide-angle dual-band tunable graphene metamaterial perfect absorber with T-shaped strips and square ring," Phys. Scripta **97**, 025507 (2022).
20. J. Guo, "A polarization-insensitive dual-band terahertz absorber using triangle graphene metamaterial structure," Microw. Opt. Technol. Lett. **64**, 1958–1964 (2022).
21. S. Yin, Z. Zhu, X. Gao, Q. Wang, J. Yuan, Y. Liu, and L. Jiang, "Terahertz nonreciprocal and functionality-switchable devices based on dielectric multilayers integrated with graphene and VO_2," Opt. Lett. **47**, 678–681 (2022).
22. X. Zhu and B. Wang, "Graphene-based angle insensitive and tunable single band and dual band metamaterial terahertz absorber," Phys. Status Solidi B **259**, 2100573 (2021).
23. P. Jordan, J. V. Neumann, and E. P. Wigner, "On an algebraic generalization of the quantum mechanical formalism," Ann. Math. **35**, 29–64 (1934).
24. F. Monticone and A. Alù, "Bound states within the radiation continuum in diffraction gratings and the role of leaky modes," New J. Phys. **19**, 093011 (2017).
25. N. A. Cumpsty and D. S. Whitehead, "The excitation of acoustic resonances by vortex shedding," J. Sound Vib. **18**, 353–369 (1971).
26. A. G. Every and A. A. Maznev, "Fano line shapes of leaky surface acoustic waves extending from supersonic surface wave points," Wave Motion **79**, 1–9 (2018).
27. L. Ni, Z. Wang, C. Peng, and Z. Li, "Tunable optical bound states in the continuum beyond in-plane symmetry protection," Phys. Rev. B **94**, 245148 (2016).
28. Y. Kivshar, "Resonant tunneling and bound states in the continuum," Low Temp. Phys. **48**, 389–395 (2022).
29. P. Vaity, H. Gupta, A. Kala, S. D. Gupta, Y. S. Kivshar, V. R. Tuz, and V. G. Achanta, "Polarization-independent quasibound states in the continuum," Adv. Photon. Res. **3**, 2100144 (2021).
30. G. Zograf, K. Koshelev, A. Zalogina, V. Korolev, R. Hollinger, D. Y. Choi, M. Zuerch, C. Spielmann, B. Luther-Davies, D. Kartashov, S. V. Makarov, S. S. Kruk, and Y. Kivshar, "High-harmonic generation from resonant dielectric metasurfaces empowered by bound states in the continuum," ACS Photon. **9**, 567–574 (2022).
31. M. V. Rybin, K. L. Koshelev, Z. F. Sadrieva, K. B. Samusev, A. A. Bogdanov, M. F. Limonov, and Y. S. Kivshar, "High-Q supercavity modes in subwavelength dielectric resonators," Phys. Rev. Lett. **119**, 243901 (2017).
32. H. M. Doeleman, F. Monticone, W. den Hollander, A. Alù, and A. F. Koenderink, "Experimental observation of a polarization vortex at an optical bound state in the continuum," Nat. Photonics **12**, 397–401 (2018).
33. E. Gao, H. Li, Z. Liu, C. Xiong, C. Liu, B. Ruan, M. Li, and B. Zhang, "Investigation of bound states in the continuum in dual-band perfect absorbers," Opt. Express **30**, 14817–14827 (2022).
34. S. I. Azzam, V. M. Shalaev, A. Boltasseva, and A. V. Kildishev, "Formation of bound states in the continuum in hybrid plasmonic-photonic systems," Phys. Rev. Lett. **121**, 253901 (2018).
35. L. Cong and R. Singh, "Symmetry-protected dual bound states in the continuum in metamaterials," Adv. Opt. Mater. **7**, 1900383 (2019).
36. X. Wang, S. Li, and C. Zhou, "Polarization-independent toroidal dipole resonances driven by symmetry-protected BIC in ultraviolet region," Opt. Express **28**, 11983–11989 (2020).

37. C. Ma, Q. Lin, L. Wang, and K. Huang, "Highly tunable dual bound states in the continuum in bulk Dirac semimetal metasurface," Appl. Phys. Express **14**, 042002 (2021).
38. Z. Cheng, X. Luo, L. Xu, X. Zhai, and L. Wang, "Complete optical absorption in hybrid halide perovskites based on critical coupling in the communication band," Opt. Express **28**, 14151–14161 (2020).
39. J. R. Piper and S. Fan, "Total absorption in a graphene monolayer in the optical regime by critical coupling with a photonic crystal guided resonance," ACS Photon. **1**, 347–353 (2014).
40. C. Liu, H. Li, H. Xu, M. Zhao, C. Xiong, M. Li, B. Ruan, B. Zhang, and K. Wu, "Plasmonic biosensor based on excellently absorbable adjustable plasmon-induced transparency in black phosphorus and graphene metamaterials," New J. Phys. **22**, 073049 (2020).
41. M. Li, H. Li, H. Xu, C. Xiong, M. Zhao, C. Liu, B. Ruan, B. Zhang, and K. Wu, "Dual-frequency on-off modulation and slow light analysis based on dual plasmon-induced transparency in terahertz patterned graphene metamaterial," New J. Phys. **22**, 103030 (2020).
42. B. Ruan, C. Liu, C. Xiong, M. Li, B. Zhang, E. Gao, K. Wu, and H. Li, "Absorption and self-calibrated sensing based on tunable Fano resonance in a grating coupled graphene/waveguide hybrid structure," J. Lightwave Techn. **39**, 5657–5661 (2021).
43. H. Xu, X. Wang, Z. Chen, X. Li, L. He, Y. Dong, G. Nie, and Z. He, "Optical tunable multifunctional slow light device based on double monolayer graphene grating-like metamaterial," New J. Phys. **23**, 123025 (2021).
44. R. Zhou, J. Peng, S. Yang, D. Liu, Y. Xiao, and G. Cao, "Lifetime and nonlinearity of modulated surface plasmon for black phosphorus sensing application," Nanoscale **10**, 18878–18891 (2018).
45. Y. Yi, Z. Yi, F. Zhao, H. Yang, M. Li, B. Wu, E. Gao, Y. Yi, and M. Long, "Independently tunable triple-band infrared perfect absorber based on the square loops-shaped nano-silver structure," Phys. E **139**, 115122 (2022).
46. X. Zhang, F. Zhou, Z. Liu, Z. Zhang, Y. Qin, S. Zhuo, X. Luo, E. Gao, and H. Li, "Quadruple plasmon-induced transparency of polarization desensitization caused by the Boltzmann function," Opt. Express **29**, 29387–29401 (2021).
47. H. Chen, Z. Chen, H. Yang, L. Wen, Z. Yi, Z. Zhou, B. Dai, J. Zhang, X. Wu, and P. Wu, "Multi-mode surface plasmon resonance absorber based on dart-type single-layer graphene," RSC Adv. **12**, 7821–7829 (2022).
48. R. Cheng, Y. Zhou, J. Liu, S. Hu, H. Liu, J. Pan, W. Huang, X. He, B. Liang, and L. Zhang, "Independently tunable multi-band terahertz absorber based on graphene sheet and nanoribbons," Opt. Express **30**, 3893–3902 (2022).
49. C. Xiong, H. Xu, M. Zhao, B. Zhang, C. Liu, B. Zeng, K. Wu, B. Ruan, M. Li, and H. Li, "Triple plasmon-induced transparency and outstanding slow-light in quasi-continuous monolayer graphene structure," Sci. China Phys. Mech. **64**, 224211 (2020).
50. H. Xu, Z. He, Z. Chen, G. Nie, and H. Li, "Optical Fermi level-tuned plasmonic coupling in a grating-assisted graphene nanoribbon system," Opt. Express **28**, 25767–25777 (2020).
51. E. Gao, H. Li, Z. Liu, C. Xiong, C. Liu, B. Ruan, M. Li, and B. Zhang, "Terahertz multifunction switch and optical storage based on triple plasmon-induced transparency on a single-layer patterned graphene metasurface," Opt. Express **28**, 40013–40023 (2020).
52. Z. Liu, X. Zhang, F. Zhou, X. Luo, Z. Zhang, Y. Qin, S. Zhuo, E. Gao, H. Li, and Z. Yi, "Triple plasmon-induced transparency and optical switch desensitized to polarized light based on a mono-layer metamaterial," Opt. Express **29**, 13949–13959 (2021).
53. S. Balci, O. Balci, N. Kakenov, F. B. Atar, and C. Kocabas, "Dynamic tuning of plasmon resonance in the visible using grapheme," Opt. Lett. **41**, 1241–1244 (2016).
54. Y. Todorov, A. M. Andrews, I. Sagnes, R. Colombelli, P. Klang, G. Strasser, and C. Sirtori, "Strong light-matter coupling in subwavelength metal-dielectric microcavities at terahertz frequencies," Phys. Rev. Lett. **102**, 186402 (2009).
55. S. X. Xia, X. Zhai, L. L. Wang, and S. C. Wen, "Plasmonically induced transparency in double-layered graphene nanoribbons," Photon. Res. **6**, 692–702 (2018).
56. W. Gao, J. Shu, C. Qiu, and Q. Xu, "Excitation of plasmonic waves in graphene by guided-mode resonances," ACS Nano **6**, 7806–7813 (2012).
57. H. Friedrich and D. Wintgen, "Interfering resonances and bound states in the continuum," Phys. Rev. A **32**, 3231–3242 (1985).
58. A. Christ, S. G. Tikhodeev, N. A. Gippius, J. Kuhl, and H. Giessen, "Waveguide-plasmon polaritons: strong coupling of photonic and electronic resonances in a metallic photonic crystal slab," Phys. Rev. Lett. **91**, 183901 (2003).
59. S. G. Tikhodeev, N. A. Gippius, A. Christ, T. Zentgraf, J. Kuhl, and H. Giessen, "Waveguide-plasmon polaritons in photonic crystal slabs with metal nanowires," Phys. Status Solidi C **2**, 795–800 (2005).
60. J. Hu, E. Yao, W. Xie, W. Liu, D. Li, Y. Lu, and Q. Zhang, "Strong longitudinal coupling of Tamm plasmon polaritons in graphene/DBR/Ag hybrid structure," Opt. Express **27**, 18642–18652 (2019).
61. S. G. Lee, S. H. Kim, and C. S. Kee, "Bound states in the continuum (BIC) accompanied by avoided crossings in leaky-mode photonic lattices," Nanophotonics **9**, 4373–4380 (2020).
62. D. K. Efetov and P. Kim, "Controlling electron-phonon interactions in graphene at ultrahigh carrier densities," Phys. Rev. Lett. **105**, 256805 (2010).
63. T. Sang, J. Gao, L. Wang, H. Qi, X. Yin, and Y. Wang, "Numerical study of angle-insensitive and tunable dual-band THz absorber using periodic cross-shaped graphene arrays," Materials **12**, 2063 (2019).
64. T. Klar, M. Perner, S. Grosse, G. Von Plessen, W. Spirkl, and J. Feldmann, "Surface-plasmon resonances in single metallic nanoparticles," Phys. Rev. Lett. **80**, 4249–4252 (1998).